Fracture roughness in three-dimensional beam lattice systems

Phani K. V. V. Nukala and Pallab Barai
Computer Science and Mathematics Division, Oak Ridge National Laboratory, Oak Ridge, Tennessee 37831-6164, USA

Stefano Zapperi
CNR-IENI, Via R. Cozzi 53, 20125 Milano, Italy and ISI Foundation, Viale S. Severo 65, 10133 Torino, Italy

Mikko J. Alava
Department of Engineering Physics, Aalto University, FIN-02015 Aalto, Finland

Srđan Šimunović
Computer Science and Mathematics Division, Oak Ridge National Laboratory, Oak Ridge, Tennessee 37831-6164, USA

(Received 25 March 2010; published 4 August 2010)

We study the scaling of three-dimensional crack roughness using large-scale beam lattice systems. Our results for prenotched samples indicate that the crack surface is statistically isotropic, with the implication that experimental findings of anisotropy of fracture surface roughness in directions parallel and perpendicular to crack propagation is not due to the scalar or vectorial elasticity of the model. In contrast to scalar fuse lattices, beam lattice systems do not exhibit anomalous scaling or an extra dependence of roughness on system size. The local and global roughness exponents (ζ_{loc} and ζ, respectively) are equal to each other, and the three-dimensional crack roughness exponent is estimated to be $\zeta_{loc}=\zeta=0.48\pm0.03$. This closely matches the roughness exponent observed outside the fracture process zone. The probability density distribution $p[\Delta h(\ell)]$ of the height differences $\Delta h(\ell)=[h(x+\ell)-h(x)]$ of the crack profile follows a Gaussian distribution, in agreement with experimental results.

DOI: 10.1103/PhysRevE.82.026103 PACS number(s): 62.20.mm, 46.50.+a, 62.25.Mn

I. INTRODUCTION

The scaling properties of fracture surfaces have been intensely studied in the last two decades [1,2]. Experiments on several materials under different loading conditions have shown that the fracture surfaces are self-affine [3], which implies that if the in-plane length scales of a fracture surface are scaled by a factor λ then the out-of-plane length scales (height) of the fracture surface scale by λ^{ζ}, where ζ is the roughness exponent. These experiments include metals [4], glass [5], rocks [6], and ceramics [7], which originally indicated a universal out-of-plane roughness exponent of $\zeta \simeq 0.8$ for three-dimensional (3D) fracture surfaces irrespective of the material studied (see Ref. [8] for a review). Recent experimental evidence shows, however, that the picture is more complicated: such a scaling is valid at small and intermediate scales in the so-called fracture process zone (FPZ) where elastic interactions are screened, while at large scales one observes a new regime with $\zeta \simeq 0.45$ [9,10]. This result is attributed to large-scale dynamics of a fracture front, when elasticity competes with disorder [11,12]. Although such theories of pinning and depinning of crack fronts resolve many of the mysteries of the observed regimes of self-affinity [13], a quantitative theory explaining these different exponents in the two regimes of fracture is still missing.

The theoretical understanding of the origin and universality of crack surface roughness is often investigated by discrete lattice (fuse, central-force, and beam) models [2]. In these models the elastic medium is described by a network of discrete elements such as fuses, springs, and beams with random failure thresholds. In the simplest approximation of a scalar displacement, one recovers the random fuse model (RFM) where a lattice of fuses with random threshold is subject to an increasing external voltage [14]. Early simulations using three-dimensional RFM obtained contradictory results for the crack surface roughness exponents, i.e., $\zeta=0.62\pm0.05$ [15] and $\zeta=0.41\pm0.02$ [16,17]. Recently, using large system sizes (up to $L=64$) with extensive sample averaging, we found that the crack roughness exhibits anomalous scaling [18] with $\zeta_{loc}=0.4\pm0.03$ and $\zeta=0.52\pm0.03$ [19].

It should be noted that the roughness exponent estimated using three-dimensional fuse and Born models is close to the $\zeta \simeq 0.45$ exponent measured in sandstone and glass ceramics experiments [9,10]. However, the original intent of these models was to be able to capture the $\zeta \simeq 0.8$ roughness exponent measured in various materials, but so far none of the numerical models have been successful in this. One possibility suggested for this is the inadequacy of fuse models in that they are a scalar representation of elasticity. In this sense, fuse models are analogous to the mode-III fracture. On the other hand, spring and beam models are better suited for vectorial representation of elasticity, and hence are expected to provide better estimates of roughness exponent at both short and large scales of fracture. In particular, the beam model should represent a discretized version of a Cosserat continuum. Simulations using three-dimensional Born (spring) models resulted in crack surface roughness exponent of $\zeta=0.5$ [20], in close comparison with the results obtained using the three-dimensional fuse models. At this point, it is not clear whether the same roughness exponent of $\zeta=0.5$ results from the three-dimensional beam models or the agreement between fuse and spring models is an artifact of soft modes in the spring models.

In addition to this inadequacy of fuse models in computing the $\zeta \simeq 0.8$ roughness exponent, these models have also been inadequate in capturing the anisotropic roughness scaling of the fracture surfaces as observed in typical recent experiments [21,22]. In these, anisotropy was discovered as the roughness exponent measured along the crack front direction ζ_y was found to be different from the roughness exponent measured along the crack propagation direction ζ_x. In particular, at length scale smaller that the size of the FPZ the reported values are $\zeta_y = 0.8$ and $\zeta_x = 0.6$, while in the large-scale regime the two values are close to each other [21].

In some cases it has been argued that fracture surfaces exhibit anomalous scaling [18]: the *global* exponent describing the scaling of the crack width with the sample size is larger than the local exponent measured on a single sample [23,24]. In this sense, it is necessary to introduce two roughness exponents, a global exponent (ζ) and a local exponent (ζ_{loc}), measuring the global scaling with sample size and the local scaling with observation scale. Anomalous scaling is also noted in experiments in which fracture roughness evolved as a function of distance from the initial notch [25]; however, its origin is not clear yet although in experiments it is conjectured to be an artifact of initial transient regime as the fracture front moves away from the initial notch [22,25]. In addition, anomalous scaling is only observed in samples with an extended FPZ, while it is absent otherwise.

The questions we address in this paper are the following: (i) whether anisotropic surface roughness can be captured by three-dimensional fracture simulations using the beam lattice systems when a crack propagates from a preset notch; (ii) whether anomalous scaling is present in these 3D beam lattice fracture simulations and, if it exists, then, is it because of initial transient regime close to the initial notch; and (iii) finally, what is the roughness exponent and what is its relation to those obtained using simplified scalar RFM and Born models. This paper has three further sections: in the next one, we describe the beam model used. In Sec. III, we present the numerical results obtained with it. Finally, Sec. IV concludes the paper.

II. BEAM MODEL

The random threshold beam model (RBM) we consider in this study is a three-dimensional cubic lattice system of size $L \times L \times L$. Unlike the scalar RFM model, the vectorial RBM has six degrees of freedom (x, y, z translations and three rotations about x, y, z axes) at each of the lattice nodes (sites), and each of the bonds (beams) in the lattice connects two nearest-neighbor nodes [2,26,27]. We assume that the beams are connected rigidly at each of the nodes such that the angle between any two beams connected at a node remains unaltered during the deformation process (see Fig. 1). These nodal displacements and rotations introduce conjugate forces and bending moments in the beam members.

In the RBM, we start with a fully intact lattice system with beams having unit length, unit square cross section, and Young's modulus $E=1$. This results in a unit axial stiffness ($EA/\ell_b = 1$) and bending stiffness ($12EI/\ell_b^3 = 1$) for each of the beams in the lattice system. Since the beam can deform

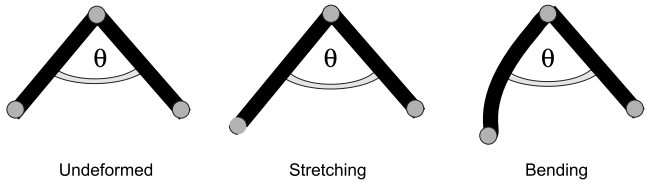

FIG. 1. Beams are connected rigidly at each of the nodes. The angle θ between two beams remains unaltered during the deformation that can be due to stretching or bending.

in two independent deformation modes (axial and bending), we assume randomly distributed bond breaking axial and bending thresholds, t_a and t_b, based on threshold probability distributions $p_a(t_a)$ and $p_b(t_b)$, respectively. The failure criterion for a beam is defined through an axial force and an effective bending moment interaction equation given by

$$r \equiv \left(\frac{F}{t_a}\right)^2 + \frac{\max(|M_i|,|M_j|)}{t_b} = 1, \tag{1}$$

where F is the axial force, and M_i and M_j are effective bending moments at nodes i and j, respectively. An effective bending moment at node i is defined as $M_i = \sqrt{(M_{xi}^2 + M_{yi}^2 + M_{zi}^2)}$. The beam breaks irreversibly whenever the failure criterion $r \geq 1$. The criterion used is the same as in Ref. [27], while one could in principle use other choices in the RBM (which has more degrees of freedom than scalar models and offers thus other alternatives such as simple thresholds for axial and bending forces or the energy of the beam). Periodic boundary conditions are imposed in the horizontal direction and a constant unit displacement difference is applied between the top and the bottom of lattice system.

Numerically, a unit displacement, $\Delta = 1$, is applied at the top of the lattice system and the equilibrium equations for force and momenta (see the Appendix for details) are solved to determine the force in each of the beams, resulting in global displacements and rotations $\mathbf{d}$. Using these values, local displacements $\mathbf{d}_\ell = \mathbf{T}\mathbf{d}$ and local forces $\mathbf{F}_\ell = \mathbf{K}_{local}\mathbf{d}_\ell$ are computed for each of the intact beams. Subsequently, for each bond k with nodes i and j, the quantities $a_k = (F/t_a)^2$ and $b_k = \max(|M_i|,|M_j|)/t_b$ are evaluated, and the bond k_c having the smallest value,

$$r_k = \frac{-b_k + \sqrt{b_k^2 + 4a_k}}{2a_k}, \tag{2}$$

is irreversibly removed (when $a_k = 0$, then $r_k = 1/b_k$). The forces are redistributed instantaneously after a bond is broken implying that the stress relaxation in the lattice system is much faster than the breaking of a bond. Each time a bond is broken, it is necessary to re-equilibrate the lattice system in order to determine the subsequent breaking of a bond. The process of breaking of a bond, one at a time, is repeated until the lattice system falls apart. For the RBM, we consider a uniform probability distribution in [0,1] for both axial and bending thresholds disorders, $p_a(t_a)$ and $p_b(t_b)$, respectively (i.e., $p(t) = 1$ for t in [0,1] and zero otherwise).

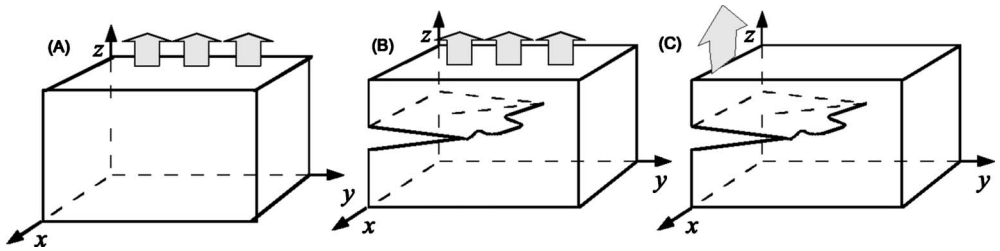

FIG. 2. The three sets of conditions used in the simulations.

Numerical simulation of fracture using large beam networks is often hampered due to the high computational cost associated with solving a new large set of linear equations every time a new lattice bond is broken. Although the sparse direct solvers presented in [28] are superior to iterative solvers in two-dimensional (2D) lattice systems, for 3D lattice systems, the memory demands brought about by the amount of fill-in during the sparse Cholesky factorization favor iterative solvers. Hence, iterative solvers are in common use for large-scale 3D lattice simulations. However, even with our state-of-the-art block-circulant preconditioned conjugate gradient iterative scheme [29], serial simulation of a large-scale 3D beam system is cumbersome due to severe computational requirements posed by 3D beam simulations. Consequently, we use massively parallel version of this algorithm on state-of-the-art computational resources at the Oak Ridge National Laboratory. The architectural details for this supercomputer can be found in [30].

Using this numerical algorithm, we investigated fracture of large 3D cubic lattice systems (e.g., $L=64$), which is so far the largest lattice system considered. For many lattice system size, we consider large numbers of sample configurations to reduce the statistical error in the numerical results.

III. CRACK ROUGHNESS

In the following, we investigate the roughness of crack profiles obtained from RBM simulations. Those are done under three different conditions: (A) an intact sample under plate loading, (B) a notched sample under plate loading, and (C) a notched sample under line loading (see Fig. 2). In particular, we investigate whether the roughness computed based on these crack profiles exhibits anisotropic and/or anomalous scaling.

A. Un-notched simulations

Once the sample has failed, we identify the final fracture surface by removing the dangling ends and overhangs as shown in Fig. 3. Let the height of the fracture surface be $h(x,y)$, where $x \in [0,L]$ and $y \in [0,L]$. In the case of notched simulations presented later, the x direction represents the crack propagation direction and the y direction represents the crack front direction. For computing crack width along the x direction, we consider local width of crack lines $h_y(x) = h(x,y=c)$ and average over different $y=c$ values. A similar computation of crack lines $h_x(y)=h(x=c,y)$ along the y direction is considered for computing crack widths along the y direction. Thus, the crack roughness in the x direction is computed by considering the roughness of $L+1$ number of slices each with $h(x,y=c)$, where c is a constant that takes on values $c=1,2,\ldots,L+1$. Once the crack line roughness of each of these $L+1$ lines with $h(x,y=c)$ is computed, the crack surface roughness in the x direction is estimated as the average roughness of these $L+1$ crack lines, which is then averaged over different realizations. Similarly, the crack surface roughness in the y direction is computed as the average roughness of the $L+1$ crack lines $h(x=c,y)$, where c is a constant that takes on values $c=1,2,\ldots,L+1$ for each of $L+1$ slices, respectively.

The local width along the x direction, $w_x(\ell) \equiv \langle \Sigma_x [h_y(x) - (1/\ell)\Sigma_X h_y(X)]^2 \rangle^{1/2}$, where the sums are restricted to regions of length ℓ and the average is over different realizations, scales as $w_x(\ell) \sim \ell_x^{\zeta}$ for $\ell \ll L$, and saturates to a value $W_x = w_x(L) \sim L_x^{\zeta}$ corresponding to the global width. Similarly, $w_y(\ell) \equiv \langle \Sigma_y [h_x(y) - (1/\ell)\Sigma_Y h_x(Y)]^2 \rangle^{1/2}$ and scales as $w_y(\ell) \sim \ell_y^{\zeta}$ for $\ell \ll L$. Global width along the y direction scales as $W_y = w_y(L) \sim L_y^{\zeta}$. The power spectrum $S_x(k) \equiv \langle \hat{h}_{y_k} \hat{h}_{y_{-k}} \rangle / L$, where $\hat{h}_{y_k} \equiv \Sigma_x h_y(x) \exp i(2\pi x k/L)$, decays as $S_x(k) \sim k^{-(2\zeta_x+1)}$. A similar result $S_y(k) \sim k^{-(2\zeta_y+1)}$ is obtained for power spectrum in the y direction. When anomalous scaling is present [18,23,24], the exponent describing the system size dependence of the surface *differs* from the local exponent measured for a fixed system size L. In particular, the local width scales as $w_x(\ell) \sim \ell^{\zeta_{loc-x}} L^{\zeta_x - \zeta_{loc-x}}$, so that the global

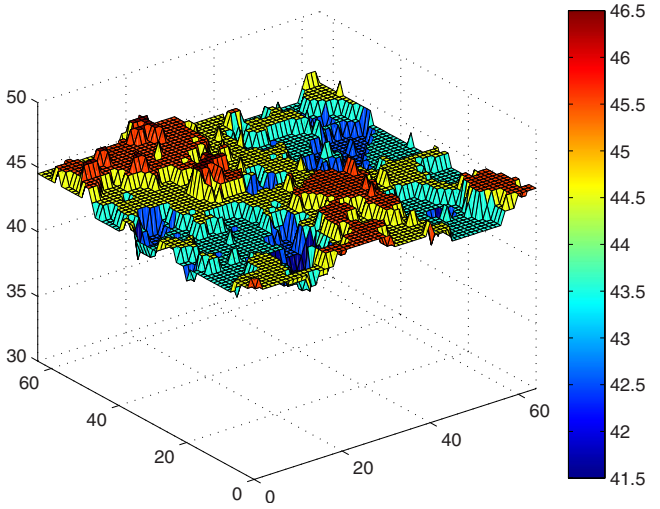

FIG. 3. (Color online) A typical fracture surface in a system of size $L \times L \times L$ with $L=64$.

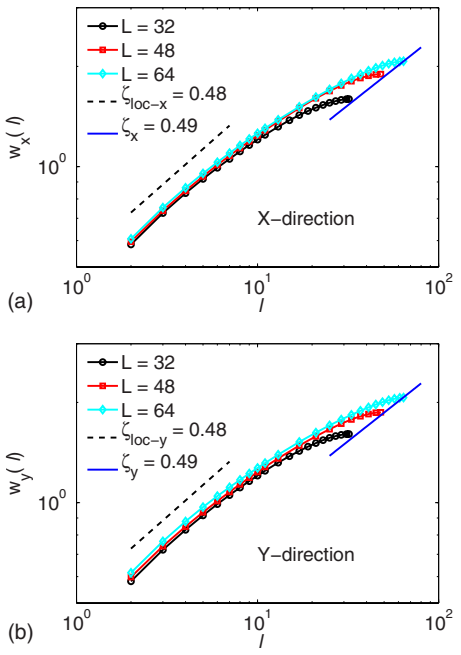

FIG. 4. (Color online) (a) Scaling of crack width $w_x(\ell)$ with window size ℓ in the x direction. (b) Scaling of crack width $w_y(\ell)$ with window size ℓ in the y direction. The local and global roughness exponents in both x and y directions are obtained as $\zeta_{loc-x}=\zeta_{loc-y}=0.48$ and $\zeta_x=\zeta_y=0.49$, respectively, which indicate isotropy of the fracture surface roughness. Moreover, unlike the fuse model, anomalous scaling is not present in the three-dimensional beam model.

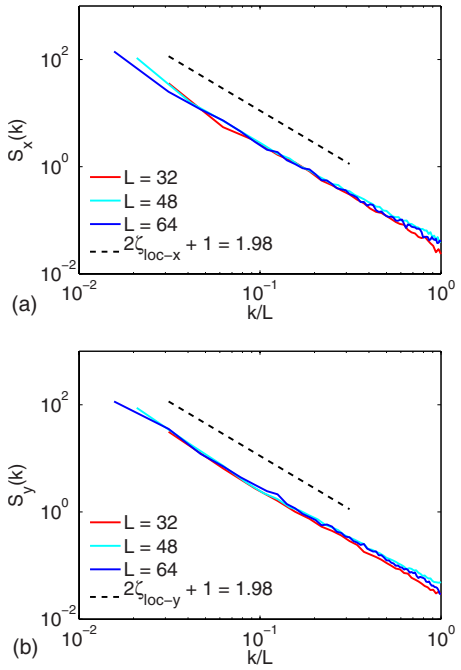

FIG. 5. (Color online) (a) Scaling of power spectrum in the x direction $S_x(k)$. (b) Scaling of power spectrum in the y direction $S_y(k)$. The local roughness exponent obtained from the slope of these power spectrum plots is consistent with the values shown in Fig. 4.

roughness W scales as L_x^{ζ} with $\zeta_x > \zeta_{loc-x}$. Consequently, the power spectrum scales as $S_x(k) \sim k^{-(2\zeta_{loc-x}+1)} L^{2(\zeta_x-\zeta_{loc-x})}$.

Figure 4 presents the scaling of local crack width in the x and y directions for different window sizes ℓ. The results presented in Figs. 4(a) and 4(b) indicate isotropic crack width scaling in the x and y directions, and the local roughness exponents are $\zeta_{loc-x}=\zeta_{loc-y}=0.48$. The fitting of the global width with L indicates a global roughness exponent of $\zeta_x=\zeta_y=0.49$, very close to the local exponents. Thus, in contrast with 3D fuse models, anomalous roughness is not a feature of fracture surfaces obtained using 3D RBM models. The power spectra of crack profiles $S_x(k)$ and $S_y(k)$ in both x and y directions in Figs. 5(a) and 5(b) imply collapsed local roughness exponents consistent with those obtained in Fig. 4, with further proof for isotropy of RBM fracture surfaces and the absence of anomalous scaling of roughness.

In the following, we investigate the probability density $p[\Delta h(\ell)]$ of height differences $\Delta h(\ell)$. In Refs. [31–34], the $p[\Delta h(\ell)]$ distribution is shown to follow a Gaussian distribution in 2D samples above a cutoff length scale and the deviations away from Gaussian distribution in the tails of the distribution have been attributed to finite jumps in the crack profiles (see Ref. [35] also). A self-affine scaling of $p[\Delta h(\ell)]$ implies that the cumulative distribution $P[\Delta h(\ell)]$ scales as $P[\Delta h(\ell)] \sim P[\Delta h(\ell)/\langle \Delta h^2(\ell)\rangle^{1/2}]$. Figures 6(a) and 6(b) present the cumulative probability distributions $P[\Delta h(\ell)]$ of the height differences $\Delta h(\ell)$ in both x and y directions on a normal or Gaussian paper for bin sizes $\ell \ll L$. The data indicate that the Gaussian distribution is adequate as the $P[\Delta h(\ell)]$ data collapse onto a straight line on a normal paper for all the window sizes between $\ell=[2-L/2]$. In the 2D RBM model, we noted that the distribution is not Gaussian for small bin sizes due to jumps in the crack profiles [35]. The same might be true even for simulations using the 3D RBM model. However, the tendency for jumps appears to be lower in three dimensions.

B. Notched simulations

In this section, we investigate whether 3D beam model simulations of notched samples exhibit anisotropic fracture surface roughness. Figure 7 presents a typical fracture surface obtained in a notched sample using 3D beam model. As can be seen in the figure, crack propagates in a parallel plane at the beginning and then roughens in the later stages due to material disorder in the failure thresholds. In contrast to 2D simulations, here a_0 measures the extent of the notch in the x direction while the notch length equals L in the y direction.

Roughness of notched surfaces is computed in a manner similar to the un-notched fracture surfaces except that in the notched cases, we do not consider the initial notch in the calculations. Figure 8 presents the scaling of local widths $w_{x/y}(\ell)$ for varying window sizes ℓ. Based on the data presented in these figures, we obtained the local and global roughness exponents in x and y directions as $\zeta_{loc-x}=\zeta_{loc-y}=0.45$ and $\zeta_x=\zeta_y=0.49$, respectively. Once again, the local exponents ζ_{loc-x} in the x direction are similar to ζ_{loc-y} in the y direction. We have also investigated the fracture surface roughness using the power spectrum method as shown in Fig. 9. Local exponents in both x and y directions are once

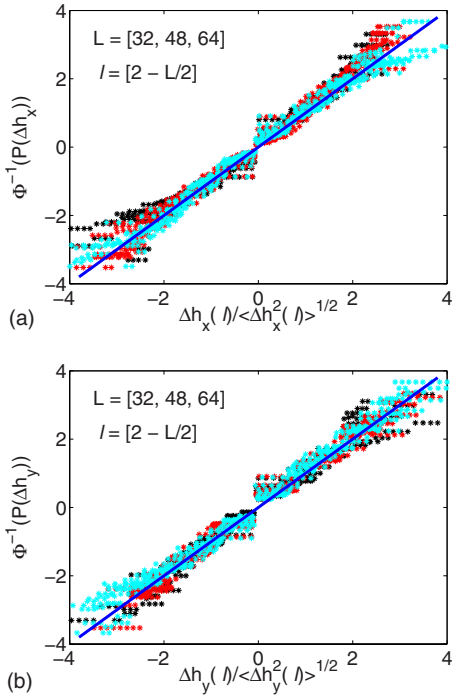

FIG. 6. (Color online) Normal paper plots of cumulative probability distributions $P[\Delta h_{x/y}(\ell)]$ of the height differences $\Delta h_{x/y}(\ell) = [h(x/y+\ell) - h(x/y)]$ of the crack profile $h(x/y)$ for various bin sizes ℓ. x/y implies either x or y and Φ^{-1} denotes inverse Gaussian. The collapse of the profiles onto a straight line with unit slope would indicate that a Gaussian distribution is adequate to represent $P[\Delta h_{x/y}(\ell)]$. (a) Values along the x direction. (b) Values along the y direction. A total of 31 data sets with data coming from three system sizes $L=(32,48,64)$ and varying window lengths between $\ell = [2-L/2]$ are plotted in (a) and (b).

again estimated to be $\zeta_{loc-x/y}=0.5$, which are in close agreement with those obtained using local width calculations. Equality of local roughness exponents in both x and y directions suggests that fracture surface anisotropy is absent even in the notched sample simulations. They also agree with the global exponents.

Figure 10 presents the probability density $p[\Delta h(\ell)]$ of height differences $\Delta h(\ell)$ for notched simulations. The data indicate that the Gaussian distribution is adequate as the $P[\Delta h(\ell)]$ data collapse onto a straight line on a normal paper

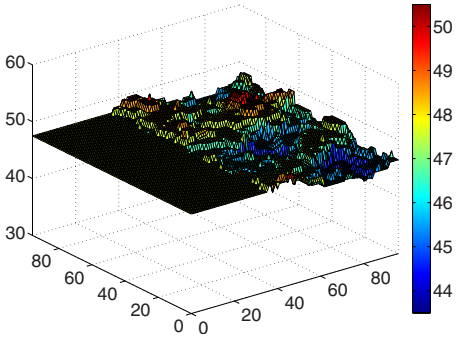

FIG. 7. (Color online) A typical fracture surface in a notched system of size $L \times L \times L$ with $L=96$ and notch size $a_0=36$.

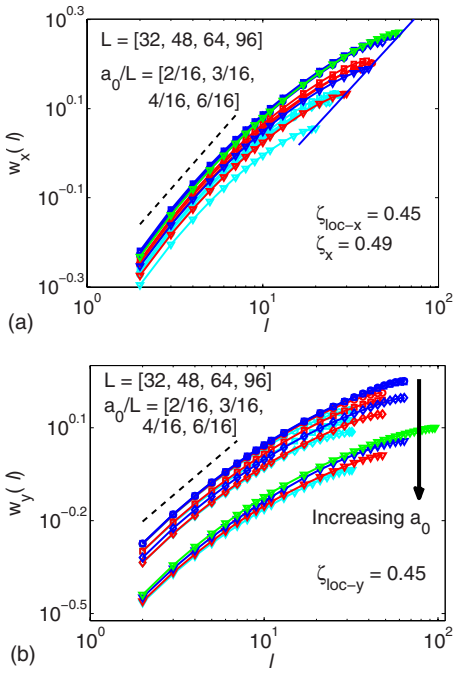

FIG. 8. (Color online) (a) Scaling of crack width $w_x(\ell)$ with window size ℓ in the x direction. (b) Scaling of crack width $w_y(\ell)$ with window size ℓ in the y direction. The values of crack width $w_{x/y}(\ell)$ are plotted for different lattice sizes of $L=[32,48,64,96]$ and for different initial notch lengths $a_0/L = [2/16, 3/16, 4/16, 6/16]$. Uniform displacement loading at the top of the lattice is applied to generate the crack surface. The local and global roughness exponents in x and y directions are obtained as $\zeta_{loc-x}=\zeta_{loc-y}=0.45$ and $\zeta_x=\zeta_y=0.49$, respectively. Same local exponents in x and y directions indicate the absence of fracture surface roughness anisotropy even for notched samples. Moreover, both local and global exponents are similar; therefore, anomalous scaling is absent in simulations using 3D beam models. Also, note that crack width $w_y(\ell)$ decreases with increasing initial notch size (a_0/L).

for all the window sizes between $\ell = [2-(L-a_0)/2]$. The collapse of the data even for small window sizes ℓ is in agreement with the observation that there are not many jumps in the 3D fracture surfaces.

In the following, we investigate how the roughness evolves away from the notch tip. As shown in Fig. 7, in the beginning, fracture propagation occurs along the notch plane for some distance and then passes through into a stable self-affine crack regime. This is clearly seen in Fig. 11, which presents scaling of crack width $w_y(\ell)$ in the y direction (crack front direction) as a function of distance d from the crack tip. The crack width remains zero until a distance d_0 away from the initial notch tip a_0. This is followed by a transient regime over which the crack width increases with distance d and then enters a stable propagation regime over which crack width remains constant with respect to distance d from the initial crack tip. This behavior in crack widths $w_y(\ell)$ remains the same irrespective of the window sizes ℓ and initial notch sizes a_0/L. Note that the data do not follow a scaling using d as "time" such that $w_y \propto d^{\beta}$, with β as a "growth exponent." Figure 12 presents a collapse of the data

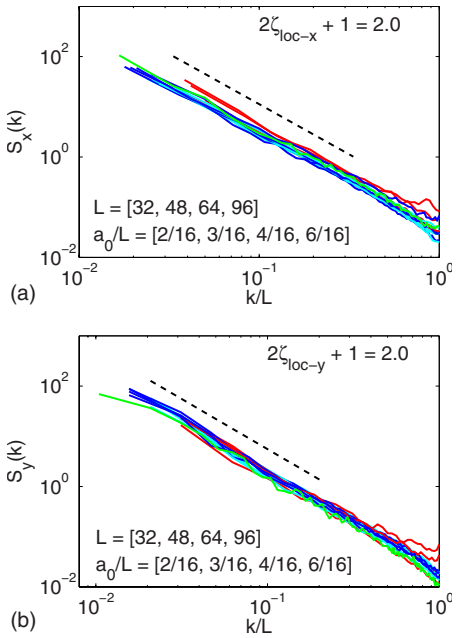

FIG. 9. (Color online) (a) Scaling of power spectrum in the x direction $S_x(k)$. (b) Scaling of power spectrum in the y direction $S_y(k)$. The data are presented for different lattice system sizes $L=[32,48,64,96]$ with initial notches of $a_0/L=[2/16,3/16,4/16,6/16]$. Local roughness exponents are estimated as $\zeta_{loc-x/y}=0.5$, which are close to the values obtained from the crack width analysis (Fig. 8).

shown in Fig. 11, which shows that the data can be collapsed for moderate to large window sizes ($\ell > 8$) while for small sizes the data do not collapse possibly because of jumps in the crack profiles.

Finally, the evolution of roughness exponent ζ_{loc-y} with distance d from the initial notch tip is presented in Fig. 13. As can be expected, the local roughness exponent is zero in the smooth fracture surface regime (where the fracture oc-

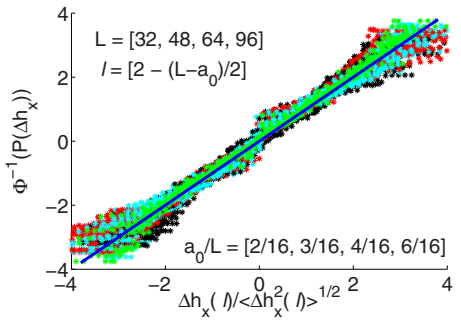

FIG. 10. (Color online) Normal paper plots of cumulative probability distributions $P[\Delta h_y(\ell)]$ of the height differences $\Delta h_y(\ell)=[h(x+\ell)-h(x)]$ of the crack profile for various bin sizes ℓ. Φ^{-1} denotes inverse Gaussian. The data are for four different lattice sizes $L=[32,48,64,96]$ with initial notch lengths $a_0/L=[2/16,3/16,4/16,6/16]$. Different window sizes ℓ were used: $\ell \in [2-(L-a_0)/2]$. The collapse of the profiles onto a straight line with unit slope would indicate that a Gaussian distribution is adequate to represent $P[\Delta h_y(\ell)]$. A similar collapse of the data is observed for crack profiles in y direction.

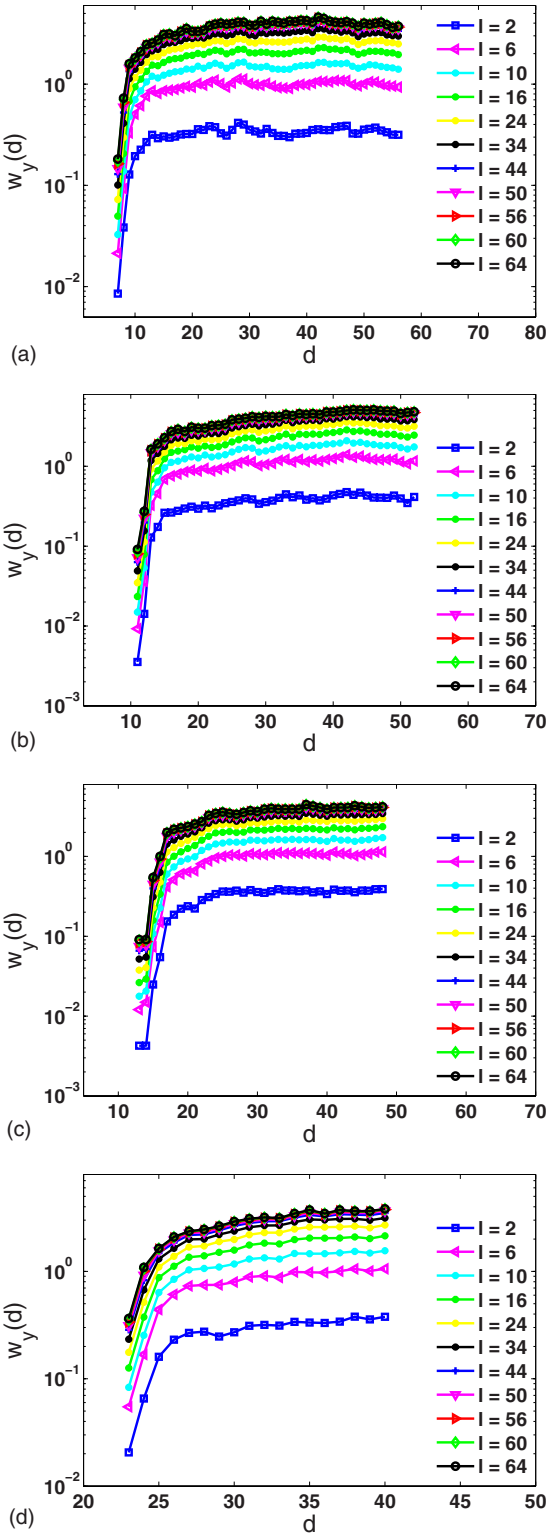

FIG. 11. (Color online) Crack width $w_y(d)$ is plotted for different initial notch sizes of a $64\times64\times64$ lattice system. Notch sizes are (a) $a_0/L=2/16$, (b) $a_0/L=3/16$, (c) $a_0/L=4/16$, and (d) $a_0/L=6/16$. The steep transition from zero width to the asymptotic value of the crack width indicates that the transient regime is small and the crack enters stable regime quite quickly. The asymptotically flat profile of the crack width for various values of d (distance from the notch tip) indicates that the proportionality constant A does not depend on d beyond the initial transient regime.

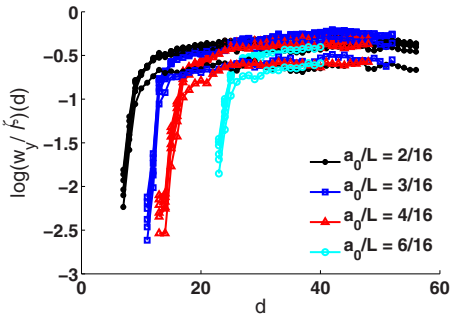

FIG. 12. (Color online) In Fig. 11 we concluded that the proportionality constant A does not depend on the distance from the notch tip d. Here, all the crack width values are collapsed by normalizing them with respect to ℓ^{ζ}. The values for larger scales ($\ell > 8$) almost collapse on each other. The crack width for window size ℓ smaller than that ($2 < \ell < 8$) does not collapse with the other values possibly because of jumps in the profiles.

curs in the notch plane). This is then followed by a jump (through a short transition regime) to stable crack propagation regime over which the roughness exponent remains constant.

C. Notched simulations with edge loading

In the previous section, we considered notched simulations with uniformly distributed loading. The only difference between simulations done in this section and the simulations done in the previous section is that, in this section, we investigate whether crack surface roughness anisotropy can be captured using 3D beam lattice model subjected to edge loading since we anticipate that edge loading is more conducive for directional crack propagation. In the edge loading, we apply concentrated loads along the line defined by $x=0$ (i.e., along the y direction representing crack front direction).

Figure 14 presents the roughness estimation of crack surface using the power spectrum method. These data indicate that the local exponent in the x direction (along the crack propagation direction) is $\zeta_{loc-x}=0.45$, while a roughness exponent of $\zeta_{loc-y}=0.43$ is obtained along the crack front direction. Moreover, we computed the roughness exponents using the crack width method and found that these results are in close agreement with those observed in power spectrum analysis.

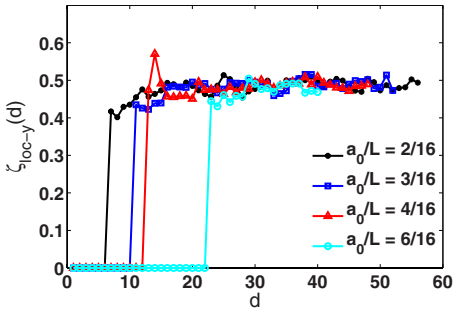

FIG. 13. (Color online) The local roughness exponent along the y direction ζ_{loc-y} is plotted as a function of the distance d from the notch tip. The data are for a lattice system of size $64\times64\times64$ averaged over 11 samples with four different initial notch sizes $a_0/L=[2/16,3/16,4/16,6/16]$. For all the four initial notch sizes the crack surface can be divided into two parts: a smooth fracture surface regime (zero roughness exponent) followed by self-affine fracture surface regime. The local roughness exponent remains almost constant in this self-affine fracture regime.

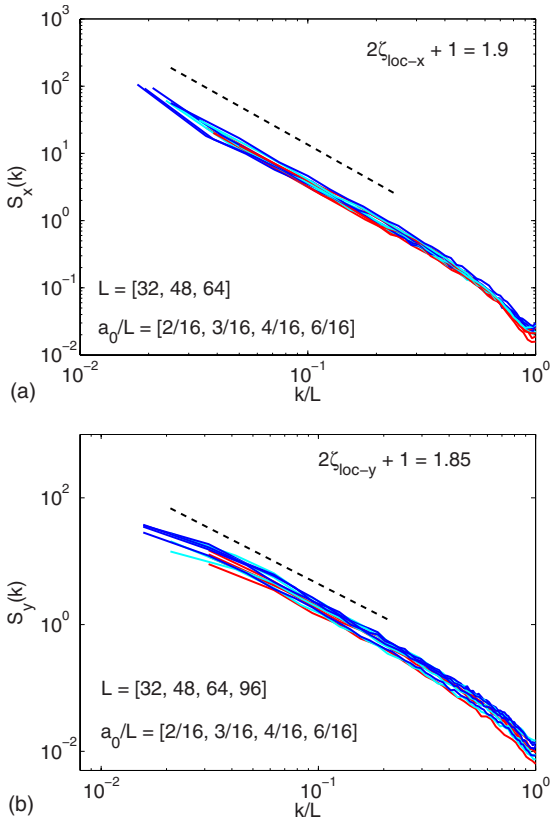

FIG. 14. (Color online) (a) Scaling of power spectrum in the x direction, $S_x(k)$. (b) Scaling of power spectrum in the y direction, $S_y(k)$. The data are presented for different lattice system sizes $L=[32,48,64]$ with initial notches of $a_0/L=[2/16,3/16,4/16,6/16]$. Local roughness exponents are estimated as $\zeta_{loc-x}=0.45$ and $\zeta_{loc-y}=0.43$, which are close to the values obtained from the crack width analysis.

Similar to earlier analysis for uniformly loaded samples, we have also analyzed the evolution of crack width $w_y(\ell)$ for edge loaded simulations. Figure 15 presents the collapsed data for various effective crack lengths that show the evolution of crack width $w_y(\ell)$ in the y direction (crack front direction) as a function of distance d from the crack tip under edge loading condition. As before, even in the edge loading samples, fracture propagates along the notch plane for some distance d_0 away from the initial crack tip a_0. The fracture then passes through into a stable self-affine crack surface through a transition regime where the crack width increases with distance d. In the stable crack propagation region, the crack width $w_y(\ell)$ remains almost constant for all values of distance d. These results are similar to those observed for uniformly distributed loading case. The collapse of the data in Fig. 15 is not perfect however; the crack width $w_y(\ell)$ scaling at small length scales ($2 < \ell < 8$) does not collapse with those at larger length scales ($\ell > 8$), possibly because of jumps in the crack profile.

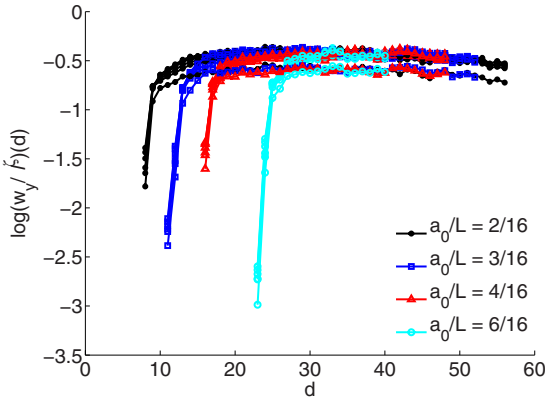

FIG. 15. (Color online) Crack width $w_y(d)$ values at different distance from the notch tip is plotted by normalizing them with respect to ℓ^{ζ} under edge loading for different initial notch sizes $a_0/L=[2/16,3/16,4/16,6/16]$. Similar to Fig. 11 for uniformly distributed loading, here under concentrated edge loading the crack width values $w_y(d)$ for larger scales ($\ell>8$) almost collapse on each other. For window size ℓ smaller than that ($2<\ell<8$), the crack width does not collapse probably due to the presence of jumps in the smaller length scales.

The effect of different initial notch sizes a_0/L on the roughness exponent ζ_{loc-y} along the y direction as a function of distance d under concentrated edge loading is presented in Fig. 16. Similar to the crack surface under uniformly distributed loading, the local roughness exponent is zero at short distances away from the notch tip and transitions to a stable value $\zeta_{loc-y}\sim 0.45$ away from the notch tip.

IV. DISCUSSION

In summary, the analysis and results presented in this paper indicate that crack profiles obtained in fracture simulations using the 3D beam lattice systems neither exhibit anomalous scaling of roughness nor exhibit the anisotropy of fracture surface roughness. The local roughness exponents in both x and y directions are estimated to be $\zeta_{loc-x}=\zeta_{loc-y}=0.48$, while the global roughness exponents are estimated to be $\zeta_x=\zeta_y=0.49$. This has important implications since the RBM is a true representation of elasticity in a Cosserat medium and should be valid for materials with a microstructure.

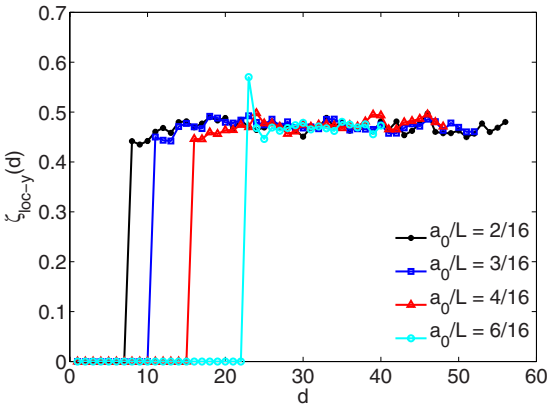

FIG. 16. (Color online) The local roughness exponent along the y direction ζ_{loc-y} under concentrated edge loading is plotted as a function of the distance d from the notch tip, similar to Fig. 13 for uniformly distributed loading. The data are for a lattice system of size $64\times64\times64$ averaged over 20 samples with four different initial notch sizes $a_0/L=[2/16,3/16,4/16,6/16]$. Equivalent to its uniformly distributed loading counterpart, under edge loading as well, for all the four initial notch sizes the crack surface can be divided into a smooth fracture surface regime with zero roughness exponent followed by self-affine fracture surface regime with constant local roughness exponent.

Comparing the result to other models (RFM and Born models) with signs of anomalous scaling, one sees nevertheless indications of similar roughness scaling [19,20]. As mentioned earlier, anomalous scaling may be due to rare large jumps in the crack profiles in these models. Leaving aside the anomalous scaling issue, the similarity in the local roughness exponent between the beam, spring, and possibly fuse models is interesting to note because of these model's dissimilarity in representing deformation of an elastic medium. This seems to imply that the anisotropy in the stress redistribution in tensorial models is irrelevant for the roughness, even in three dimensions (Ref. [35] showed that it is irrelevant in two dimensions).

The results of our simulations are best discussed in the framework of existing theories for crack roughness. From the numerical point of view our results are not far, but apparently distinct, from the prediction of crack depinning models [13], suggesting that $\zeta\simeq0.4$. In the past, there has been a debate about the equivalence between crack surface and minimum-energy surfaces [15–17,36], predicting $\zeta=0.43$. Recently, this equivalence has been put into question in two dimensions since the mapping does not work even for perfectly plastic fuses, originally thought to be an exact realization of minimum-energy surfaces [37]. The present results appear as well to be distinct from minimum-energy surfaces. Furthermore, a scaling argument relates the roughness exponent to the percolation correlation exponent [38]. It was argued that the exponent should differ for the beam model and the RFM. Here, we found that the exponent is instead the same for the two models. The main conclusion of the present paper is that the roughness exponent is the same regardless of the type of elasticity employed and is close to $\zeta=0.5$, without any noticeable anisotropy.

Finally, it is interesting to conclude about the relation of the current simulations to depinning theory of line cracks in three dimensions and to experimental evidence. The equality of the exponents with and without notch might possibly be taken to imply that the roughness exponent in the (large) notch simulations arises from internal roughening inside a fracture process zone (FPZ). This would then explain why the exponents do not adhere to those valid for large- or short-scale regimes in experiments, and the theoretical counterparts—when existent. It is a pertinent open question what is "missing" in the RBM simulations so as to not match depinning predictions, and likewise it is a valid question as to what kind of a model would describe the roughening seen here. For the first of these, one may speculate about the role of disorder, and whether we can see with the accessible system sizes the asymptotic scaling regime—in other words if there would be a crossover from the "FPZ" to continuum behavior. Note however that even in that case the short-range FPZ exponents are again different from experiments.

ACKNOWLEDGMENTS

This research was sponsored by the Mathematical, Information and Computational Sciences Division, Office of Advanced Scientific Computing Research, U.S. Department of Energy under Contract No. DE-AC05-00OR22725 with UT-Battelle, LLC. M.J.A. and S.Z. gratefully thank the financial support of the European Commissions NEST Pathfinder program TRIGS under Contract No. NEST-2005-PATH-COM-043386. M.J.A. also acknowledges the financial support from The Center of Excellence program of the Academy of Finland.

APPENDIX: DETAILS ABOUT THE BEAM MODEL

In the RBM model, beams are connected rigidly at each of the nodes and the angle between any two beams remains unaltered during the deformation process. These nodal displacements and rotations introduce conjugate forces and bending moments. Using Timoshenko beam theory [39], which includes shear deformations of the beam cross section in addition to the usual axial deformation of cross sections, the *local* stiffness matrix for a beam element that relates the local nodal displacements and rotations to local nodal forces and bending moments in the beam's local coordinate system is given by

$$
\mathbf{K}_{local} = \begin{bmatrix}
\frac{EA}{\ell_b} & 0 & 0 & 0 & 0 & 0 & -\frac{EA}{\ell_b} & 0 & 0 & 0 & 0 & 0 \\
 & \frac{12EI_z}{(1+\alpha_y)\ell_b^3} & 0 & 0 & 0 & \frac{6EI_z}{(1+\alpha_y)\ell_b^2} & 0 & -\frac{12EI_z}{(1+\alpha_y)\ell_b^3} & 0 & 0 & 0 & \frac{6EI_z}{(1+\alpha_y)\ell_b^2} \\
 & & \frac{12EI_y}{(1+\alpha_z)\ell_b^3} & 0 & -\frac{6EI_y}{(1+\alpha_z)\ell_b^2} & 0 & 0 & 0 & -\frac{12EI_y}{(1+\alpha_z)\ell_b^3} & 0 & -\frac{6EI_y}{(1+\alpha_z)\ell_b^2} & 0 \\
 & & & \frac{GJ}{\ell_b} & 0 & 0 & 0 & 0 & 0 & -\frac{GJ}{\ell_b} & 0 & 0 \\
 & & & & \frac{(4+\alpha_z)EI_y}{(1+\alpha_z)\ell_b} & 0 & 0 & 0 & \frac{6EI_y}{(1+\alpha_z)\ell_b^2} & 0 & \frac{(2-\alpha_z)EI_y}{(1+\alpha_z)\ell_b} & 0 \\
 & & & & & \frac{(4+\alpha_y)EI_z}{(1+\alpha_y)\ell_b} & 0 & -\frac{6EI_z}{(1+\alpha_y)\ell_b^2} & 0 & 0 & 0 & \frac{(2-\alpha_y)EI_z}{(1+\alpha_y)\ell_b} \\
 & & & & & & \frac{EA}{\ell_b} & 0 & 0 & 0 & 0 & 0 \\
 & & & & & & & \frac{12EI_z}{(1+\alpha_y)\ell_b^3} & 0 & 0 & 0 & -\frac{6EI_z}{(1+\alpha_y)\ell_b^2} \\
 & & & & SYM & & & \frac{12EI_y}{(1+\alpha_z)\ell_b^3} & 0 & \frac{6EI_y}{(1+\alpha_z)\ell_b^2} & 0 & \\
 & & & & & & & & \frac{GJ}{\ell_b} & 0 & 0 & \\
 & & & & & & & & & \frac{(4+\alpha_z)EI_y}{(1+\alpha_z)\ell_b} & 0 & \\
 & & & & & & & & & & \frac{(4+\alpha_y)EI_z}{(1+\alpha_y)\ell_b} &
\end{bmatrix},
$$

where E is the Young's modulus; G is the shear modulus; A is the beam cross-sectional area; I_y and I_z are the moments of inertia of the beam cross section with respect to y and z axes, respectively; ℓ_b is the length of the beam; and J is the torsion constant of the beam. $\alpha_y = 12EI_z/GA\ell_b^2$ and $\alpha_z = 12EI_y/GA\ell_b^2$ are the shear correction factors, which denote the ratio of bending stiffness to the shear stiffness. If shear deformation of beam cross section is negligible, then $\alpha_y = \alpha_z = 0$ and the Timoshenko beam theory reduces to Euler-Bernoulli beam theory. Equation (A1) presents a relation between local nodal displacements and rotations $\mathbf{d}_\ell = (u_{li}, v_{li}, w_{li}, \theta_{lxi}, \theta_{lyi}, \theta_{lzi}, u_{lj}, v_{lj}, w_{lj}, \theta_{lxj}, \theta_{lyj}, \theta_{lzj})^T$ and local forces and moments $\mathbf{F}_\ell = (F_{lxi}, F_{lyi}, F_{lzi}, M_{lxi}, M_{lyi}, M_{lzi}, F_{lxj}, F_{lyj}, F_{lzj}, M_{lxj}, M_{lyj}, M_{lzj})^T$. In this setting, the subscript l refers to local quantities, the superscript T represents transpose of a vector or a matrix, i and j refer to ith and

*j*th nodes of the beam, and F and M refer to force and bending moments, respectively.

Computing the equilibrium of the lattice system is achieved by first transforming these local quantities ($\mathbf{d}_\ell$ and $\mathbf{F}_\ell$) into global quantities $\mathbf{d}=(u_i,v_i,w_i,\theta_{xi},\theta_{yi},\theta_{zi},u_j,v_j,w_j,\theta_{xj},\theta_{yj},\theta_{zj})^T$ and $\mathbf{F}=(F_{xi},F_{yi},F_{zi},M_{xi},M_{yi},M_{zi},F_{xj},F_{yj},F_{zj},M_{xj},M_{yj},M_{zj})^T$ through a coordinate transformation $\mathbf{T}$ such that $\mathbf{d}_\ell=\mathbf{T}\mathbf{d}$, $\mathbf{F}_\ell=\mathbf{T}\mathbf{F}$, and $\mathbf{K}=\mathbf{T}^T\mathbf{K}_{local}\mathbf{T}$, and then satisfying equilibrium equations at each node such that

$$\Sigma_{\langle ij\rangle}F_x=0,\quad \Sigma_{\langle ij\rangle}F_y=0,\quad \Sigma_{\langle ij\rangle}F_z=0, \tag{A2}$$

$$\Sigma_{\langle ij\rangle}M_x=0,\quad \Sigma_{\langle ij\rangle}M_y=0,\quad \Sigma_{\langle ij\rangle}M_z=0, \tag{A3}$$

where $\Sigma_{\langle ij\rangle}$ implies that the summation is carried over all the intact bonds $\langle ij\rangle$ joining at node i. In the above discussion, the transformation matrix $\mathbf{T}$ is given by

$$\mathbf{T}=\begin{bmatrix}\mathbf{Q} & \mathbf{0} & \mathbf{0} & \mathbf{0}\\ \mathbf{0} & \mathbf{Q} & \mathbf{0} & \mathbf{0}\\ \mathbf{0} & \mathbf{0} & \mathbf{Q} & \mathbf{0}\\ \mathbf{0} & \mathbf{0} & \mathbf{0} & \mathbf{Q}\end{bmatrix}, \tag{A4}$$

where $\mathbf{Q}$ is an orthogonal global to local transformation.

[1] *Statistical Models for the Fracture of Disordered Media*, edited by H. J. Herrmann and S. Roux (North-Holland, Amsterdam, 1990).

[2] M. J. Alava, P. K. V. V. Nukala, and S. Zapperi, Adv. Phys. **55**, 349 (2006).

[3] B. B. Mandelbrot, D. E. Passoja, and A. J. Paullay, Nature (London) **308**, 721 (1984).

[4] K. J. Måløy, A. Hansen, E. L. Hinrichsen, and S. Roux, Phys. Rev. Lett. **68**, 213 (1992); E. Bouchaud, G. Lapasset, J. Planés, and S. Navéos, Phys. Rev. B **48**, 2917 (1993).

[5] P. Daguier, B. Nghiem, E. Bouchaud, and F. Creuzet, Phys. Rev. Lett. **78**, 1062 (1997).

[6] J. Schmittbuhl, S. Roux, and Y. Berthaud, EPL **28**, 585 (1994); J. Schmittbuhl, F. Schmitt, and C. Scholz, J. Geophys. Res. **100**, 5953 (1995).

[7] J. J. Mecholsky, D. E. Passoja, and K. S. Feinberg-Ringel, J. Am. Ceram. Soc. **72**, 60 (1989).

[8] For a review see, E. Bouchaud, J. Phys.: Condens. Matter **9**, 4319 (1997); Surf. Rev. Lett. **10**, 797 (2003).

[9] J. M. Boffa, C. Allain, and J. Hulin, Eur. Phys. J. AP **2**, 281 (1998).

[10] L. Ponson, H. Auradou, M. Pessel, V. Lazarus, and J.-P. Hulin, Phys. Rev. E **76**, 036108 (2007).

[11] D. Bonamy, L. Ponson, S. Prades, E. Bouchaud, and C. Guillot, Phys. Rev. Lett. **97**, 135504 (2006).

[12] D. Dalmas, A. Lelarge, and D. Vandembroucq, Phys. Rev. Lett. **101**, 255501 (2008).

[13] D. Bonamy, J. Phys. D **42**, 214014 (2009).

[14] L. de Arcangelis, S. Redner, and H. J. Herrmann, J. Phys. (Paris), Lett. **46**, 585 (1985).

[15] G. G. Batrouni and A. Hansen, Phys. Rev. Lett. **80**, 325 (1998).

[16] V. I. Räisänen, M. J. Alava, and R. M. Nieminen, Phys. Rev. B **58**, 14288 (1998).

[17] V. I. Räisänen, E. T. Seppälä, M. J. Alava, and P. M. Duxbury, Phys. Rev. Lett. **80**, 329 (1998).

[18] J. M. López, M. A. Rodríguez, and R. Cuerno, Phys. Rev. E **56**, 3993 (1997).

[19] Phani Kumar V. V. Nukala, S. Zapperi, and S. Simunovic, Phys. Rev. E **74**, 026105 (2006).

[20] A. Parisi, G. Caldarelli, and L. Pietronero, EPL **52**, 304 (2000).

[21] L. Ponson, D. Bonamy, and E. Bouchaud, Phys. Rev. Lett. **96**, 035506 (2006).

[22] L. Ponson, D. Bonamy, H. Auradou, G. Mourot, S. Morel, E. Bouchaud, C. Guillot, and J. P. Hulin, Int. J. Fract. **140**, 27 (2006).

[23] J. M. López and J. Schmittbuhl, Phys. Rev. E **57**, 6405 (1998).

[24] S. Morel, J. Schmittbuhl, J. M. López, and G. Valentin, Phys. Rev. E **58**, 6999 (1998).

[25] G. Mourot, S. Morel, E. Bouchaud, and G. Valentin, Phys. Rev. E **71**, 016136 (2005).

[26] S. Roux and E. Guyon, J. Phys. (Paris), Lett. **46**, 999 (1985).

[27] H. J. Herrmann, A. Hansen, and S. Roux, Phys. Rev. B **39**, 637 (1989).

[28] Phani Kumar V. V. Nukala and S. Simunovic, J. Phys. A **36**, 11403 (2003).

[29] Phani Kumar V. V. Nukala and S. Simunovic, J. Phys. A **37**, 2093 (2004).

[30] NCCS, Jaguar's system architecture, http://www.nccs.gov/computing-resources/jaguar

[31] L. I. Salminen, M. J. Alava, and K. J. Niskanen, Eur. Phys. J. B **32**, 369 (2003).

[32] M. J. Alava, P. K. V. V. Nukala, and S. Zapperi, J. Stat. Mech.: Theory Exp. (2006) L10002.

[33] Jan Oystein Haavig Bakke, T. Ramstad, and A. Hansen, Phys. Rev. B **76**, 054110 (2007).

[34] S. Santucci, K. J. Maloy, A. Delaplace, J. Mathiesen, A. Hansen, Jan Oistein Haavig Bakke, J. Schmittbuhl, L. Vanel, and P. Ray, Phys. Rev. E **75**, 016104 (2007).

[35] P. K. V. V. Nukala, S. Zapperi, M. J. Alava, and S. Simunovic, Phys. Rev. E **78**, 046105 (2008).

[36] A. Hansen, E. L. Hinrichsen, and S. Roux, Phys. Rev. Lett. **66**, 2476 (1991).

[37] C. B. Picallo, J. M. López, S. Zapperi, and M. J. Alava, Phys. Rev. Lett. **103**, 225502 (2009).

[38] A. Hansen and J. Schmittbuhl, Phys. Rev. Lett. **90**, 045504 (2003).

[39] J. S. Przemieniecki, *Theory of Matrix Structural Analysis* (McGraw-Hill Book Company, New York, 1968).